

# Discovery of an Extremely Metal-Poor Galaxy at $z = 3.654$ Using JWST Infrared Spectroscopy

Sijia Cai<sup>1,\*</sup>, Zijian Yu<sup>2</sup>

<sup>1</sup> Department of Astronomy, Tsinghua University, Beijing 100084, China; [caisj23@mails.tsinghua.edu.cn](mailto:caisj23@mails.tsinghua.edu.cn)

<sup>2</sup> Blair Academy, 2 Park St, Blairstown, New Jersey 07825

Received 20XX Month Day; accepted 20XX Month Day

**Abstract** We report the discovery of an extremely metal-poor galaxy at a redshift of  $z = 3.654$ , identified through infrared spectroscopy using the James Webb Space Telescope (JWST). This galaxy, CAPERS-39810, exhibits a metallicity of  $12 + \log(\text{O}/\text{H}) = 6.73 \pm 0.13$ , indicative of its primitive chemical composition, resembling the early stages of galaxy formation in the Universe. We use JWST NIRSpec/MSA for spectroscopic analysis, complemented by photometric data from the COSMOS2025 catalog. Our analysis employs the R3 strong-line diagnostic method to estimate metallicity, due to the lack of auroral lines in the spectrum. The galaxy’s emission lines, including  $\text{H}\beta$ ,  $[\text{O III}]$ ,  $\text{H}\alpha$  and  $\text{He I}$ , are clearly detected. The rest-frame equivalent widths of the strong hydrogen recombination lines are  $\text{EW}_0(\text{H}\beta) = 184 \pm 48 \text{ \AA}$  and  $\text{EW}_0(\text{H}\alpha) = 1144 \pm 48 \text{ \AA}$ . Furthermore, we perform detailed spectral energy distribution modeling to derive a galaxy logarithmic stellar mass of  $8.02^{+0.22}_{-0.34} M_{\odot}$ . This discovery adds to the growing body of evidence for the existence of very low-metallicity galaxies existed at cosmic noon of  $z \approx 3$ , which are crucial for understanding the processes of chemical enrichment and star formation in young galaxies at the cosmic noon.

**Key words:** galaxies: general — galaxies: high-redshift — galaxies: abundances — galaxies: star formation

## 1 INTRODUCTION

The first generations of stars, commonly referred to as Population III (Pop III) stars, are thought to have formed out of metal-free primordial gas in the early Universe (Tumlinson & Shull 2000; Schaerer 2003; Bromm & Yoshida 2011). Owing to the lack of metal-line cooling, Pop III stars are predicted to reach very high stellar masses and to host extremely hard ionizing radiation fields (Klessen & Glover 2023; Nandal et al. 2025). As a consequence, observational searches have frequently focused on nebular signatures associated with such hard spectra, such as strong  $\text{He II } \lambda 1640$  emission and the absence or weakness of metal lines like  $[\text{O III}]$  (e.g., Cai et al. 2011, 2015; Wang et al. 2024; Maiolino et al. 2024; Mondal et al. 2025; Nakajima et al. 2025; Fujimoto et al. 2025). However, very massive stars evolve rapidly, and the  $\text{He II}$  emission powered by Pop III stars is expected to fade on timescales of  $\sim 3$  Myr (Schaerer

2002). Moreover, recent models predict that Pop III galaxies are likely to be rapidly “self-polluted” by the first supernova explosions (Rusta et al. 2025), yielding  $[\text{O III}]/\text{H}\beta \approx 1$ . As a result, the unambiguous identification of Pop III stellar populations remains a major open challenge for both observations and theory.

The James Webb Space Telescope (JWST) has enabled unprecedented observations of faint galaxies in the early Universe, providing new insights into the history of early star formation. Extensive JWST surveys of dwarf galaxies at  $z \sim 2$ -10 have revealed a well-defined mass-metallicity relation (MZR), with galaxies at fixed stellar mass exhibiting progressively lower metallicities toward higher redshift (Li et al. 2023; Nakajima et al. 2023; Curti et al. 2024; Sanders et al. 2024; Sarkar et al. 2025). Notably, the metallicities inferred for these systems remain above  $\sim 2\% Z_{\odot}$ , a result that has been interpreted either as evidence for rapid chemical enrichment in the early Universe (Gutcke et al. 2022) or as a consequence of observational selection biases. At the same time, however, an increasing number of recent studies have reported candidates

The authors contributed equally to this work and are listed in alphabetical order.

for extremely metal-poor galaxies (EMPGs), suggesting that this apparent “metallicity floor” may not be universal (Chemerynska et al. 2024; Hsiao et al. 2025; Willott et al. 2025; Cullen et al. 2025; Nakajima et al. 2025). In particular, several recent discoveries have highlighted compelling candidates for primordial or Pop III-hosting systems. For example, Morishita et al. (2025) identified the “AMORE6” at  $z = 5.725$  using NIRC*am* Wide Field Slitless Spectroscopy (WFSS). At somewhat lower redshifts, closer to the peak epoch of cosmic star formation, Cai et al. (2025) and Vanzella et al. (2026) reported the candidate primordial galaxies “CR3” at  $z = 3.19$  and “LAP2” at  $z = 4.19$ , respectively, based on deep NIRS*pec* spectroscopy. Together, these discoveries further complicate our understanding of the chemical enrichment history of the Universe.

In this work, we report the discovery of an extreme metal-poor galaxy at  $z=3.654$  and analyze its spectroscopy and spectral energy distribution (SED) to assess metallicity and physical conditions, placing it among the growing population of chemically primitive systems that JWST has so far uncovered. This paper is organized as follows: In Sec. 2, we describe our observations, including data selection and processing. In Sec. 3, we present our procedures for emission line flux measurements, metallicity calibrations based on strong-line diagnostics and SED fitting. Discussion and a summary of our major conclusions are detailed in Sec. 4. Throughout this work we adopt a flat  $\Lambda$ CDM cosmology consistent with Planck Collaboration et al. (2020), with  $H_0 = 67.7 \text{ km s}^{-1} \text{ Mpc}^{-1}$ ,  $\Omega_m = 0.31$ , and  $\Omega_\Lambda = 0.69$ . For the reference gas-phase metallicity scale, we assume a solar oxygen abundance of  $12 + \log(\text{O}/\text{H}) = 8.69$  from Asplund et al. (2021).

## 2 OBSERVATIONS AND DATA PROCESSING

CAPERS-39810 is located in the well-known COSMOS field (Scoville et al. 2007; Koekemoer et al. 2011; Grogin et al. 2011) at RA = 150.1335857 and Dec = 2.271014. In this work, we primarily use imaging and spectroscopic data obtained with the JWST.

### 2.1 Spectroscopy

The NIRS*pec*/MSA spectrum of CAPERS-39810 was acquired under the JWST Cycle 3 program CANDELS-Area Prism Epoch of Reionization Survey (CAPERS; GO#6368; PI: M. Dickinson). The main goal of CAPERS is to identify up to 10,000 spectroscopically confirmed galaxies at  $z > 10$  using the NIRS*pec* Prism. CAPERS-39810 was observed in Observation 10 on 15 April 2025 and Observation 4 on 19 May 2025, with 4.74 hours

of effective exposure per visit (9.48 hours in total). The raw data are retrieved from the Mikulski Archive for Space Telescopes (MAST) at the Space Telescope Science Institute. Each visit is processed independently using the official JWST pipeline (software version 1.17.1; CRDS context `jwst_1322.pmap`; Bushouse et al. 2025). The standard Level 1 and Level 2 processing steps, including the 1/f noise correction, are applied. We perform background subtraction using the standard three-shutter nodding strategy to obtain 2D spectra. Finally, 1D spectra are extracted using a box aperture with a width of six pixels, adopting the default extraction parameters. Prior to stacking, the 2D spectra are aligned along the spatial direction to match the trace position in Observation 4, and the spectral axis of both the 1D and 2D products are resampled onto the wavelength grid of Observation 4. The resampled spectra are then combined using inverse-variance weighting to produce the final stacked 1D and 2D spectra shown in Fig. 1.

### 2.2 Image and Photometry

We use publicly available imaging and photometric data from the COSMOS2025 catalog (Shuntov et al. 2025). This includes HST/ACS F814W from the COSMOS HST ACS F814W dataset (Koekemoer et al. 2007), JWST/NIRC*am* F115W, F150W, F277W, and F444W, and JWST/MIRI F770W from the 255-hour JWST Cycle 1 Treasury Program COSMOS-Web (GO#1727; PIs: J. Kartaltepe and C. Casey; Casey et al. 2023). We use the catalog photometry, which is measured in small elliptical apertures and has been corrected for Kron aperture losses and for point-spread function (PSF) effects.

## 3 METHODS AND ANALYSIS

### 3.1 Emission lines

As seen in the spectrum (Fig. 1), four emission lines are robustly detected at a significance level of greater than  $3\sigma$ , including  $\text{H}\beta$ ,  $[\text{O III}] \lambda\lambda 4959, 5007$ ,  $\text{H}\alpha$  and  $\text{He I } \lambda 10830$ . Due to limited spectral resolution, the two emission lines  $[\text{O III}] \lambda 4959$  and  $[\text{O III}] \lambda 5007$  are blended. We thus model the combined  $[\text{O III}] \lambda\lambda 4959, 5007$  profile with a single Gaussian function. Prior to line fitting, we mask the short-wavelength region (observed wavelength  $\sim 0.6\text{--}2.0 \mu\text{m}$ ), where the noise level is high. The continuum and emission lines were modeled simultaneously, with the continuum represented by a constant component and the emission lines described by Gaussian profiles. The best-fit parameters were obtained through non-linear

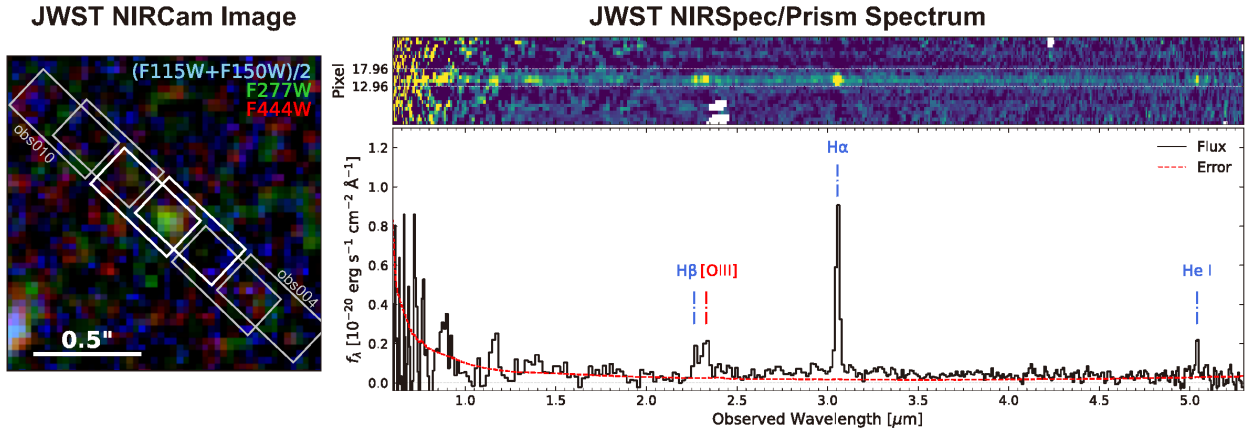


Fig. 1: JWST observations of CAPERS-39810 are shown. The left panel displays a composite RGB image constructed from JWST NIRCcam imaging, where the F444W, F277W, and the average of the F115W and F150W bands are mapped to the red, green, and blue channels, respectively. The white polygon denotes the configuration of the NIRSspec shutters. The right panel shows the stacked NIRSspec/Prism 2D spectrum together with the extracted 1D spectrum. The spectral extraction region is indicated by the white dashed lines. The black solid line and the red dashed line correspond to the measured flux and the associated uncertainty. Key emission features, including  $H\beta$ ,  $H\alpha$ ,  $He\ I\ \lambda 10830$ , and the metal line  $[O\ III]\ \lambda\lambda 4959, 5007$ , are identified.

least-squares minimization, from which the line fluxes and equivalent widths (EWs) were derived.

We measure line fluxes of  $f(H\beta) = (3.8 \pm 1.0) \times 10^{-19} \text{ erg s}^{-1} \text{ cm}^{-2}$ ,  $f([O\ III]) = (7.9 \pm 1.6) \times 10^{-19} \text{ erg s}^{-1} \text{ cm}^{-2}$ ,  $f(H\alpha) = (23.6 \pm 0.8) \times 10^{-19} \text{ erg s}^{-1} \text{ cm}^{-2}$  and  $f(He\ I) = (3.1 \pm 0.8) \times 10^{-19} \text{ erg s}^{-1} \text{ cm}^{-2}$ , with a rest-frame equivalent width of  $EW_0(H\beta) = 184 \pm 48 \text{ \AA}$ ,  $EW_0(H\alpha) = 1144 \pm 48 \text{ \AA}$  and  $EW_0(He\ I) = 152 \pm 38 \text{ \AA}$ . The measured value of all detected emission lines are listed in Table 1.

### 3.2 Gas-phase Metallicity

The most reliable and physically motivated metallicity calibration, the direct  $T_e$  method, requires measurements of key physical conditions, including the electron temperature and electron density. However, temperature-sensitive auroral lines, such as  $[O\ III]\ \lambda 4363$ , are typically faint, particularly in high-redshift EMPGs. In addition, the  $[O\ III]\ \lambda 3727$  line falls on the low-signal-to-noise blue end of the NIRSspec/Prism spectrum. Given these limitations, we instead adopt a strong-line metallicity diagnostic. In our case, the gas-phase metallicity is constrained using the  $R3 = [O\ III]\ \lambda 5007/H\beta$  ratio. The  $[O\ III]\ \lambda 5007$  line flux is estimated by adopting the theoretical  $[O\ III]\ \lambda 5007/[O\ III]\ \lambda 4959$  ratio of 2.98 (Storey & Zeippen 2000).

Following Sanders et al. (2024), we adopt the R3 extrapolation calibration, in which the gas-phase metallicity

is parameterized as a polynomial function of the strong-line ratio. The relation is given by

$$\log(R3) = 0.834 - 0.072x - 0.453x^2 \quad (1)$$

where  $x = 12 + \log(O/H) - 8.0$ . Given the double-valued nature of the R3 calibration, we adopt the low-metallicity branch based on the trend of mass-metallicity relation and the stellar mass derived from SED fitting (Sec. 3.3). We determine the metallicity of CAPERS-39810 to be  $12 + \log(O/H) = 6.73 \pm 0.13$ . We did not apply an explicit dust correction to the R3 ratio used for the metallicity estimate.  $[O\ III]\ \lambda 5007$  and  $H\beta$  are closely separated in wavelength and therefore experience nearly identical dust attenuation. Even if the reddening implied by the Balmer decrement is adopted and a standard attenuation law (Calzetti et al. 2000) is applied, the resulting change in the line ratio leads to a shift of only  $\sim 0.05$  dex in  $12 + \log(O/H)$ , which is well within the uncertainty of the metallicity estimate.

### 3.3 SED Modeling

We perform SED fitting for our extremely metal-poor galaxy using the Bayesian Analysis of Galaxies for Physical Inference and Parameter ESTimation code, *Bagpipes* (Carnall et al. 2018). The SED modeling is based on JWST/NIRCcam broad-band photometry and is used to estimate the global physical properties of the galaxy, in particular its stellar mass and approximate stellar age. Adopting photometric SED fitting also avoids the

Table 1: Emission Line Properties

Parameter	Value	Unit
$f(\text{H}\beta)$	$(3.8 \pm 1.0) \times 10^{-19}$	cgs
$f([\text{O III}] \lambda 4959, 5007)$	$(7.9 \pm 1.6) \times 10^{-19}$	cgs
$f(\text{H}\alpha)$	$(23.6 \pm 0.8) \times 10^{-19}$	cgs
$f(\text{He I } \lambda 10830)$	$(3.1 \pm 0.8) \times 10^{-19}$	cgs
$\text{EW}_0(\text{H}\beta)$	$184 \pm 48$	Å
$\text{EW}_0(\text{H}\alpha)$	$1144 \pm 48$	Å
$\text{EW}_0(\text{He I})$	$152 \pm 38$	Å
R3	$1.6 \pm 0.5$	-
$12 + \log(\text{O}/\text{H})$	$6.73 \pm 0.13$	-

Notes: Flux is given in cgs units as  $\text{erg s}^{-1} \text{cm}^{-2}$ .

additional complexity and potential systematic uncertainties associated with incorporating low signal-to-noise ratio (SNR) spectroscopic data, while remaining fully adequate for resolving the mass-metallicity degeneracy relevant to our metallicity determination.

To construct the SED model, we adopt a Kroupa (2001) initial mass function (IMF) and assume a delayed- $\tau$  star formation history (SFH), parameterized as

$$\text{SFR}(t) \propto t \exp\left(-\frac{t}{\tau}\right),$$

which allows for an initial rise followed by an exponential decline in the star formation rate. We adopt uniform priors on the model parameters, with the stellar age allowed to vary between 0.01 and 1.86 Gyr, the star formation timescale  $\tau$  between 0.03 and 1.0 Gyr, and the stellar metallicity between  $Z = 0.001$ - $1 Z_{\odot}$ . The total formed stellar mass is sampled with a logarithmic prior over the range  $\log(M_*/M_{\odot}) = 5$ -12.

For dust attenuation, we adopt the flexible attenuation law of Salim et al. (2018), which extends the Calzetti et al. (2000) prescription by allowing variations in both the slope of the attenuation curve and the strength of the 2175 Å bump. Uniform priors are adopted, with the  $V$ -band attenuation  $A_V$  allowed to vary between 0 and 2 mag, the slope parameter  $\delta$  between -1.2 and 0.4, and the UV bump strength  $B$  between 0 and 2.

For the nebular component, we use a wide prior on the ionization parameter,  $-4 < \log U < -1$ , consistent with values observed in high-redshift star-forming galaxies and expected for EMPGs. The redshift is fixed to the spectroscopic value of  $z = 3.654$ .

The posterior distributions are sampled using the *Nautilus* nested sampling algorithm (Lange 2023). The results of the SED fitting are shown in Fig. 2. We report the median values of the posterior distributions along with  $1\sigma$  uncertainties, corresponding to the 16th and 84th percentiles. The stellar mass is  $\log_{10} M_*/M_{\odot} = 8.02^{+0.22}_{-0.34}$ , the age is  $t_{\text{age}} = 0.27^{+0.33}_{-0.20}$  Gyr, the star formation rate

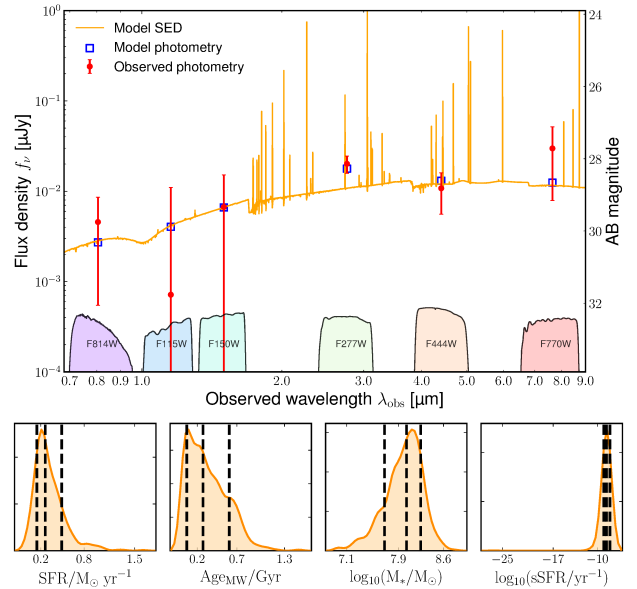


Fig. 2: SED modeling of the CAPERS-39810. The upper panel shows the results of SED fitting to the JWST NIRCam photometry. The red points represent the observed photometric measurements, while the orange curve denotes the best-fitting model SED. The blue squares overlaid on the model indicate the synthetic photometry computed from the best-fit model. The lower panel presents the posterior probability distributions of the SED model parameters. The black dashed lines mark the 16th, 50th, and 84th percentiles of the posterior distributions.

is  $\text{SFR} = 0.26^{+0.23}_{-0.12} M_{\odot} \text{yr}^{-1}$ , corresponding to a specific star formation rate of  $\log_{10}(\text{sSFR}/\text{yr}^{-1}) = -8.56^{+0.54}_{-0.43}$ . The SED fitting yields a stellar dust attenuation of  $A_V = 0.48^{+0.56}_{-0.32}$  mag.

## 4 RESULTS AND DISCUSSIONS

We report a dwarf galaxy, CAPERS-39810, at  $z = 3.654$  in the COSMOS field, enabled by the unprecedented depth of the largest NIRSpect MSA program to date, CAPERS. This source adds a new extremely metal-poor galaxy to the intermediate-redshift sample (see Fig. 3). Its NIRSpect prism spectrum shows significant detections ( $> 3\sigma$ ) of  $\text{H}\beta$ ,  $[\text{O III}] \lambda\lambda 4959, 5007$ ,  $\text{H}\alpha$ , and  $\text{He I } \lambda 10830$ . The measured line fluxes are summarized in Table 1.

Based on the SED fitting with *Bagpipes*, we derive a stellar mass of  $\log_{10} M_*/M_{\odot} = 8.02^{+0.22}_{-0.34}$ , and a stellar population age of  $t_{\text{age}} = 0.27^{+0.33}_{-0.20}$  Gyr for the target. Given its low stellar mass, we adopt the Sanders et al. (2024) R3 calibration and use the mass-metallicity relation to break the degeneracy between the upper and lower metallicity branches. This yields a gas-phase metallicity

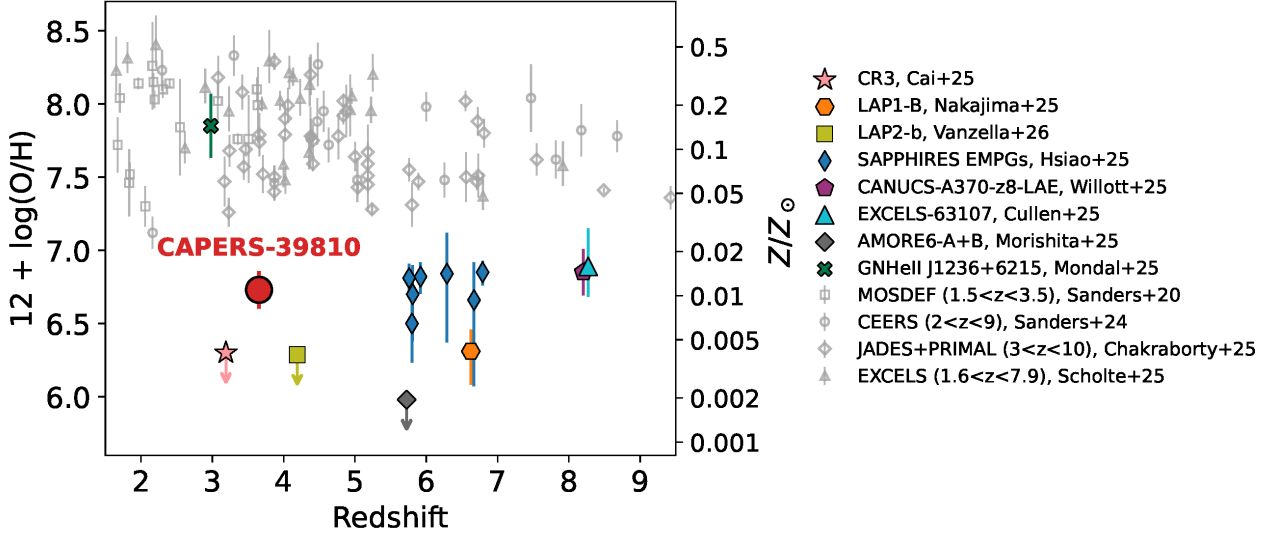


Fig. 3: Gas-phase metallicity of the CAPERS-39810. For comparison, the gray markers in the figure denote the NIRSpec samples for which metallicities have been determined using the direct  $T_e$  method (Sanders et al. 2020; Sanders et al. 2024; Chakraborty et al. 2025; Scholte et al. 2025), whereas the recently reported metal-poor galaxies are highlighted with colored markers (Cai et al. 2025; Nakajima et al. 2025; Vanzella et al. 2026; Hsiao et al. 2025; Willott et al. 2025; Cullen et al. 2025; Morishita et al. 2025; Mondal et al. 2025). All upper limits in the figure are  $1\sigma$  values.

of  $12 + \log(\text{O}/\text{H}) = 6.73 \pm 0.13$ . Additionally, using the mass-excitation (MEx) diagram reported by Coil et al. (2015), which relates R3 to stellar mass, we can rule out active galactic nuclei (AGN) contribution in this system.

The Balmer decrement derived from the observed  $\text{H}\alpha/\text{H}\beta$  implies a nebular attenuation of  $A_V^{\text{gas}} = 2.7 \pm 1.0$  assuming the Calzetti et al. (2000) attenuation law. This value is larger than the stellar attenuation inferred from the SED fitting (Section 3.3). If interpreted purely as dust reddening, the large Balmer decrement may reflect localized dust associated with recent star-forming regions rather than the global dust content of the galaxy. A patchy or clumpy dust geometry can also produce strong attenuation along particular sightlines while leaving much of the stellar continuum relatively unobscured (e.g., Wild et al. 2011). In addition, the  $\text{H}\beta$  line has relatively low SNR in the prism spectrum, and measurement uncertainties may contribute to an elevated  $\text{H}\alpha/\text{H}\beta$  ratio.

Considering the known systematic uncertainties among different metallicity calibrations, it is necessary to test multiple approaches to ensure a robust metallicity estimate. Using the calibration from Nakajima et al. (2022), whose sample includes a large number of local metal-poor galaxies, we find that our target’s  $\text{EW}_0(\text{H}\beta)$  lies near the boundary between their “medium-EW” and “large-EW” subsamples. Applying the medium-EW calibration yields  $12 + \log(\text{O}/\text{H}) = 7.08 \pm 0.15$ , whereas the large-EW calibration gives  $12 + \log(\text{O}/\text{H}) = 6.95 \pm 0.12$ . Although different calibrations introduce systematic offsets of up to

$\sim 0.3$  dex, the conclusion that our source is an extremely metal-poor galaxy remains unaffected.

CAPERS-39810 therefore represents another JWST-confirmed extremely metal-poor galaxy at intermediate redshift, following the recent discoveries reported by Cai et al. (2025) and Vanzella et al. (2026) (see Fig. 3). Fig. 4 shows the stellar mass-metallicity relation (Sanders et al. 2021; Li et al. 2023; Curti et al. 2024). CAPERS-39810 lies significantly below the MZR defined by star-forming galaxies at  $z \sim 3$ , making it a pronounced outlier relative to the bulk population. Its detection extends the census of EMPGs to the redshift range between local analogs and the numerous metal-poor systems now uncovered at  $z \gtrsim 6$  (Hsiao et al. 2025; Willott et al. 2025; Cullen et al. 2025; Morishita et al. 2025; Nakajima et al. 2025). Such extremely metal-poor systems may in fact be common throughout the Universe. However, current observational constraints make them particularly difficult to identify at intermediate redshifts. The limited survey volume of existing NIRSpec programs, the low SNR at the blue end of the prism spectra, the intrinsically faint nature of EMPGs, and the high observational cost of grating spectroscopy have collectively restricted systematic studies of EMPGs around the cosmic noon. Expanding the census of such galaxies in this epoch is essential for tracing the chemical enrichment history of the Universe, as it directly probes the conditions under which the first generations of metal-poor stars continue to form in low-mass systems.

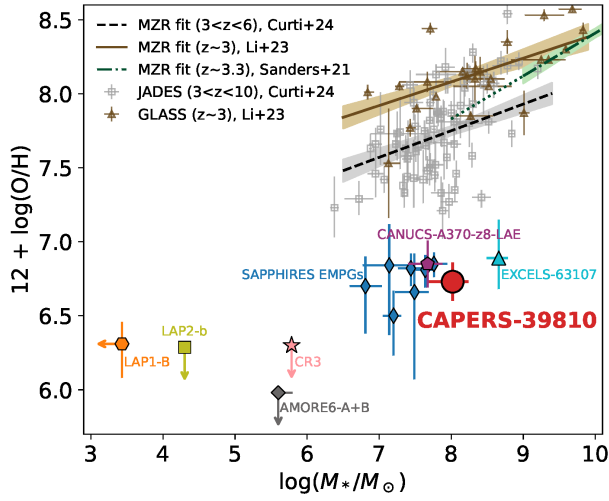


Fig. 4: The stellar mass-metallicity relation. Colored symbols denote candidate extremely metal-poor systems, corresponding to the sources highlighted in Fig. 3. The black dashed, brown solid, and dark-green dot-dashed curves show the best-fit MZR relations at  $z \sim 3$  from Curti et al. (2024), Li et al. (2023), and Sanders et al. (2021), respectively, with their  $1\sigma$  uncertainties indicated by the shaded regions; the dark-green dotted lines denote the extrapolation of the Sanders et al. (2021) relation. The overplotted gray squares and brown triangles show galaxy samples from the JWST JADES and GLASS surveys.

**Acknowledgements** We thank Prof. Zheng Cai’s supervision and encouragement of this topics, carefully reading and comment on this paper. He affirmed the contributions of our student team, and decides to remain uncredited. This work is supported by National Key R&D Program of China (grant no. 2023YFA1605600), This research is supported by National Natural Science Foundation of China (#12525303) and Tsinghua University Initiative Scientific Research Program. This work is based in part on observations made with the NASA/ESA/CSA James Webb Space Telescope. The data were obtained from the Mikulski Archive for Space Telescopes at the Space Telescope Science Institute, which is operated by the Association of Universities for Research in Astronomy, Inc., under NASA contract NAS 5-03127 for JWST. The authors acknowledge the COSMOS-Web team led by CoPIs (J. Kartaltepe and C. Casey) and CAPERS team led by PI (M. Dickinson). All the JWST raw data used in this paper can be found in MAST: 10.17909/fynv-ba75.

## References

- Asplund, M., Amarsi, A. M., & Grevesse, N. 2021, *A&A*, 653, A141 2
- Bromm, V., & Yoshida, N. 2011, *ARA&A*, 49, 373 1
- Bushouse, H., Eisenhamer, J., Dencheva, N., et al. 2025, *JWST Calibration Pipeline 2*
- Cai, S., Li, M., Cai, Z., et al. 2025, *ApJ*, 993, L52 2, 5
- Cai, Z., Fan, X., Jiang, L., et al. 2015, *ApJ*, 799, L19 1
- Cai, Z., Fan, X., Jiang, L., et al. 2011, *ApJ*, 736, L28 1
- Calzetti, D., Armus, L., Bohlin, R. C., et al. 2000, *ApJ*, 533, 682 3, 4, 5
- Carnall, A. C., McLure, R. J., Dunlop, J. S., & Davé, R. 2018, *MNRAS*, 480, 4379 3
- Casey, C. M., Kartaltepe, J. S., Drakos, N. E., et al. 2023, *ApJ*, 954, 31 2
- Chakraborty, P., Sarkar, A., Smith, R., et al. 2025, *ApJ*, 985, 24 5
- Chemerynska, I., Atek, H., Dayal, P., et al. 2024, *ApJ*, 976, L15 2
- Coil, A. L., Aird, J., Reddy, N., et al. 2015, *ApJ*, 801, 35 5
- Cullen, F., Carnall, A. C., Scholte, D., et al. 2025, *MNRAS*, 540, 2176 2, 5
- Curti, M., Maiolino, R., Curtis-Lake, E., et al. 2024, *A&A*, 684, A75 1, 5, 6
- Fujimoto, S., Asada, Y., Naidu, R. P., et al. 2025, arXiv e-prints, arXiv:2512.11790 1
- Grogin, N. A., Kocevski, D. D., Faber, S. M., et al. 2011, *ApJS*, 197, 35 2
- Gutcke, T. A., Pfrommer, C., Bryan, G. L., et al. 2022, *ApJ*, 941, 120 1
- Hsiao, T. Y.-Y., Sun, F., Lin, X., et al. 2025, arXiv e-prints, arXiv:2505.03873 2, 5
- Klessen, R. S., & Glover, S. C. O. 2023, *ARA&A*, 61, 65 1
- Koekemoer, A. M., Aussel, H., Calzetti, D., et al. 2007, *ApJS*, 172, 196 2
- Koekemoer, A. M., Faber, S. M., Ferguson, H. C., et al. 2011, *ApJS*, 197, 36 2
- Kroupa, P. 2001, *Monthly Notices of the Royal Astronomical Society*, 322, 231 4
- Lange, J. U. 2023, *MNRAS*, 525, 3181 4
- Li, M., Cai, Z., Bian, F., et al. 2023, *ApJ*, 955, L18 1, 5, 6
- Maiolino, R., Übler, H., Perna, M., et al. 2024, *A&A*, 687, A67 1
- Mondal, C., Saha, K., Borgohain, A., et al. 2025, *ApJ*, 988, 171 1, 5
- Morishita, T., Liu, Z., Stiavelli, M., et al. 2025, arXiv e-prints, arXiv:2507.10521 2, 5
- Nakajima, K., Ouchi, M., Isobe, Y., et al. 2023, *ApJS*, 269, 33 1
- Nakajima, K., Ouchi, M., Xu, Y., et al. 2022, *ApJS*, 262, 3 5
- Nakajima, K., Ouchi, M., Harikane, Y., et al. 2025, arXiv e-prints, arXiv:2506.11846 1, 2, 5

- Nandal, D., Whalen, D. J., Latif, M. A., & Heger, A. 2025, *ApJ*, 994, L11 1
- Planck Collaboration, Aghanim, N., Akrami, Y., et al. 2020, *A&A*, 641, A6 2
- Rusta, E., Salvadori, S., Gelli, V., et al. 2025, *ApJ*, 989, L32 1
- Salim, S., Boquien, M., & Lee, J. C. 2018, *ApJ*, 859, 11 4
- Sanders, R. L., Shapley, A. E., Topping, M. W., Reddy, N. A., & Brammer, G. B. 2024, *ApJ*, 962, 24 1, 3, 4, 5
- Sanders, R. L., Shapley, A. E., Reddy, N. A., et al. 2020, *MNRAS*, 491, 1427 5
- Sanders, R. L., Shapley, A. E., Jones, T., et al. 2021, *ApJ*, 914, 19 5, 6
- Sarkar, A., Chakraborty, P., Vogelsberger, M., et al. 2025, *ApJ*, 978, 136 1
- Schaerer, D. 2002, *A&A*, 382, 28 1
- Schaerer, D. 2003, *A&A*, 397, 527 1
- Scholte, D., Cullen, F., Carnall, A. C., et al. 2025, *MNRAS*, 540, 1800 5
- Scoville, N., Aussel, H., Brusa, M., et al. 2007, *ApJS*, 172, 1 2
- Shuntov, M., Akins, H. B., Paquereau, L., et al. 2025, *A&A*, 704, A339 2
- Storey, P. J., & Zeippen, C. J. 2000, *MNRAS*, 312, 813 3
- Tumlinson, J., & Shull, J. M. 2000, *ApJ*, 528, L65 1
- Vanzella, E., Messa, M., Zanella, A., et al. 2026, *A&A*, 705, L12 2, 5
- Wang, X., Cheng, C., Ge, J., et al. 2024, *ApJ*, 967, L42 1
- Wild, V., Charlot, S., Brinchmann, J., et al. 2011, *MNRAS*, 417, 1760 5
- Willott, C. J., Asada, Y., Iyer, K. G., et al. 2025, *ApJ*, 988, 26 2, 5